Measurement of turbulent velocity and bounds for thermal diffusivity in laser shock compressed foams by x-ray photon correlation spectroscopy

Charles Heaton,[1,*] Hao Yin,[2,3] Dimitri Khaghani,[4] Hae Ja Lee,[4] Hannah Poole,[1,5] Eric Blackman,[3,5,6] Nina Boiadjieva,[4] Xiaoqian M. Chen,[7] Celine Crépisson,[1] Gilbert W. Collins,[2,5,3,6] Adrien Descamps,[8] Arianna E. Gleason,[4] Christian Gutt,[9] Alexander N. Petsch,[4,10] Lisa Randolph,[11] Silke Nelson,[4] Peregrine McGehee,[4] Rajan Plumley,[4,10,12] Christopher Spindloe,[13] Thomas Stevens,[1] Charlotte Stuart,[1] Joshua J. Turner,[4,10] Hussein Aluie,[2,3,6] Jessica K. Shang,[2,3,6] and Gianluca Gregori[1]

[1]*Department of Physics, University of Oxford, Parks Road, Oxford OX1 3PU, United Kingdom*
[2]*Department of Mechanical Engineering, University of Rochester, Rochester, New York 14627, USA*
[3]*Center for Matter at Atomic Pressures, University of Rochester, Rochester, New York 14627, USA*
[4]*SLAC National Accelerator Laboratory, 2575 Sand Hill Road, Menlo Park, California 94025, USA*
[5]*Department of Physics and Astronomy, University of Rochester, New York 14627, USA*
[6]*Laboratory for Laser Energetics, University of Rochester, Rochester, New York 14623, USA*
[7]*National Synchrotron Light Source II, Brookhaven National Laboratory, Upton, New York 11973, USA*
[8]*School of Mathematics and Physics, Queens University Belfast, University Road, Belfast BT7 1NN, United Kingdom*
[9]*Department of Physics, University of Siegen, Emmy-Noether-Campus, Walter-Flex-Strasse 3, 57072 Siegen, Germany*
[10]*Stanford Institute for Materials and Energy Sciences, Stanford University, Stanford, California 94305, USA*
[11]*European XFEL, Holzkoppel 4, 22869, Schenefeld, Germany*
[12]*Department of Physics, Carnegie Mellon University, 5000 Forbes Avenue, Pittsburgh, Pennsylvania 15213, USA*
[13]*Central Laser Facility (CLF), STFC Rutherford Appleton Laboratory, Harwell Campus, Didcot OX11 0QX, United Kingdom*

(Received 15 July 2025; accepted 2 October 2025; published 29 October 2025)

Experimental benchmarking of transport coefficients under extreme conditions is required for validation of differing theoretical models. To date, measurement of transport properties of dynamically compressed samples remains a challenge with only a limited number of studies able to quantify transport in high pressure and temperature matter. x-ray photon correlation spectroscopy utilizes coherent x-ray sources to measure time correlations of density fluctuations, thus providing measurements of length and timescale-dependent transport properties. Here, we present a first-of-a-kind experiment to conduct x-ray photon correlation spectroscopy in laser shock compression experiments. We report measurement of the turbulent velocity in the wake of a laser driven supersonic shock and place an upper bound on thermal diffusivity in a solid density plasma on nanosecond timescales.

DOI: 10.1103/lff9-f3c1

I. INTRODUCTION

Transport in materials at high pressure and temperature influences a plethora of phenomena ranging from the growth rate of hydrodynamic instabilities in inertial fusion experiments [1] to melting and rotational dynamics in planetary cores [2,3]. However, there is a simultaneous lack of experimental verification of such transport properties and disagreement between theoretical predictions of transport properties as highlighted by several authors [4,5]. Experiments are therefore required to constrain theoretical models for transport in dense plasmas.

While experimental measurements of differing transport properties have been performed for statically compressed samples [6–8] there are a limited number of studies of dynamically compressed materials. Furthermore, transport coefficients from static compression experiments are unlikely to be relevant to dynamic compression experiments due to strong temperature dependence of transport properties. Recently, an investigation into thermal conductivity in driven high energy density matter at a material interface revealed the existence of anomalously suppressed thermal transport at the material boundary, so-called interfacial thermal resistance [9]. Additionally, interface tracking approaches such as those of Allen *et al.* [9] and Jiang *et al.* [10] require extensive comparison to simulation to recover transport properties and so are model-dependent. This motivates dynamic experiments that aim to characterize transport properties in bulk materials, rather than at interfaces.

X-ray photon correlation spectroscopy (XPCS) is an established diagnostic deployed at synchrotrons [11–13] and x-ray free electron lasers (XFELs) [14–16] and is the x-ray analog of dynamic light scattering [17]. Although previous experiments have performed XPCS on high pressure materials in a diamond anvil cell [18–20], here we present a first-of-a-kind

*Contact author: charles.heaton@physics.ox.ac.uk

experiment deploying XPCS on a dynamic compression experiment. When a coherent x-ray beam scatters from a sample, a speckle pattern is produced on the far field diffraction pattern. XPCS aims to recover dynamic properties of materials by linking the measured time evolution of the speckle's intensity fluctuations to density fluctuations. This is done through expressing the second order intensity-intensity autocorrelation function, $g^{(2)}(\mathbf{q}, \Delta t)$, as a function of density fluctuations through the Siegert relation [21]

$$g^{(2)}(\mathbf{q}, \Delta t) = \frac{\langle I(\mathbf{q}, t) I(\mathbf{q}, t + \Delta t)\rangle_t}{\langle I(\mathbf{q}, t)\rangle_t^2} = 1 + \beta |F(\mathbf{q}, \Delta t)|^2, \tag{1}$$

where $I(\mathbf{q}, t)$ is the intensity recorded at the scattering wavevector $\mathbf{q}$ at time t, β is the speckle visibility and $F(\mathbf{q}, \Delta t)$ is the intermediate scattering function. The operator $\langle\cdot\rangle_t$ refers to performing an ensemble average through an average over t, assuming an ergodic system. For a photon deflected by an angle θ, the momentum change of the photon is

$$\hbar|\mathbf{q}| = \hbar q = \frac{4\pi\hbar}{\lambda} \sin\left(\frac{\theta}{2}\right), \tag{2}$$

where λ is the x-ray wavelength. $F(\mathbf{q}, \Delta t)$, also referred to as the density-density autocorrelation function or the intermediate scattering function, is defined as [22]

$$F(\mathbf{q}, \Delta t) = \frac{\langle n_{\mathbf{q}}(t + \Delta t) n_{-\mathbf{q}}(t)\rangle_t}{\langle n_{\mathbf{q}}(t) n_{-\mathbf{q}}(t)\rangle_t}, \tag{3}$$

where $n_{\mathbf{q}}$ is the spatial Fourier transform of the electron density. Given that $F(\mathbf{q}, 0) = 1$, it is evident from Eq. (1) that

$$\beta(\mathbf{q}) = g^{(2)}(\mathbf{q}, 0) - 1 = \frac{\langle I(\mathbf{q}, t)^2\rangle_t}{\langle I(\mathbf{q}, t)\rangle_t^2} - 1 = \frac{\mathrm{var}(I)}{\bar{I}^2}, \tag{4}$$

where $\bar{I}$ and $\mathrm{var}(I)$ are the mean and variance of $I(\mathbf{q}, t)$. This approach is effective if a detector is able to resolve intensity fluctuations on the timescale of Δt and is deployed at synchrotrons and XFEL facilities to study dynamics down to the microsecond timescale, limited by detector readout time. However, for an application of XPCS to subnanosecond timescales, necessary for a laser shock experiment, a modified implementation of the previous approach also known as x-ray speckle visibility spectroscopy (XSVS) [23–25].

XSVS calculates $F(\mathbf{q}, \Delta t)$ by measuring a decrease in the speckle visibility or speckle contrast (β) when two pulses separated by some time, Δt, are used to probe the sample. If Δt is less than the detector readout, the detector captures the summed intensity of the two scattered pulses, $I(\mathbf{q}, t)$ and $I(\mathbf{q}, t + \Delta t)$. One can show that speckle visibility of the summed intensities, $\beta(\mathbf{q}, \Delta t)$, follows [26]

$$\beta(\mathbf{q}, \Delta t) = \frac{\beta_0}{2}(1 + |F(\mathbf{q}, \Delta t)|^2), \tag{5}$$

where β_0 is the speckle contrast expected from a single pulse scattering from a static sample. Eq. (5) is only valid for two pulses of equal intensity that are perfectly spatially overlapped. Under more realistic conditions, Sun *et al.* [25] find that

$$\beta(\mathbf{q}, \Delta t) = \beta_0[r^2 + (1 - r)^2 + 2r(1 - r)\mu|F(\mathbf{q}, \Delta t)|^2], \tag{6}$$

where $r = I_1/(I_1 + I_2)$, I_1 and I_2 are first and second the probe intensities, respectively. μ is the degree of spatial overlap. μ varies from 0 to 1 corresponding to the two pulses being completely mismatched to being perfectly overlapped, respectively.

II. EXPERIMENTAL SETUP AND METHODS

We have performed a proof of concept experiment at the Matter at Extreme Conditions (MEC) endstation at the Linac Coherent Light Source (LCLS) [27], using the two bucket mode operation [28] as shown in Fig. 1. To produce highly coherent speckle patterns, we utilize the LCLS self-seeded beam mode of operation at a central x-ray energy of 8.2 keV resulting in a high spectral bandwidth, $E/\Delta E \approx 10^{-4}$ [29]. MEC's two nanosecond drive lasers are focused onto a sample consisting of a 5 μm plastic ablator, and then a 0.15 μm gold layer to prevent preheat from x-rays and hot electrons, followed by 12.5 μm of Parylene D as a pusher, see inset of Fig. 1. This rapid ablation of the interaction foil launches a shock into the target, a 600 μm tall 0.5 g cm^{-3} trimethylolpropane triacrylate (TMPTA) foam. The foam is held within a 25 μm Kapton cylinder. The focused intensity is 11 TW cm^{-2} over a laser spot of 300 μm in a 10 ns flat top pulse. TMPTA foams are chosen due to both their application in inertial fusion energy (IFE) [30] as well as their strong scattering cross-section in the small angle x-ray scattering domain. The LCLS beam is focused down to a $\sigma = 10$ μm diameter spot 400 μm from the ablator using a stack of beryllium compound refractive lenses (CRL). In addition to the primary XPCS diagnostic, the properties of the shocked plasma were characterized by velocity interferometry (VISAR) [31], x-ray diffraction [32], and x-ray Thomson scattering [33].

Utilizing two bucket mode, LCLS can provide two pulses separated by multiples of 350 ps [28,34]. Due to shot-to-shot fluctuations in pulse intensities, we need to be able to characterize these two pulses on a single-shot basis. As indicated by Fig. 1, before the interaction point, luminescence from a 5 μm thick iron foil is recorded by a fast photodiode. This acts as a transmissive, nondisruptive, single-shot energy monitor for the two x-ray pulses. Figure 2(a) shows a measurement of the two pulses, separated by 1050 ps. We characterize the pulse intensity ratio by taking a probability distribution of x-ray only shots where, unlike laser driven shots, the signal is able to be reliably characterized. Figure 2(b) shows the distribution of pulse intensity ratios: for $\Delta t = 700$ ps $r = 0.297 \pm 0.081$ while the ratio for $\Delta t = 1050$ ps is $r = 0.218 \pm 0.062$.

Before leaving the interaction chamber, the x-ray beam is terminated by a 1 mm wide tungsten block to avoid exposing the XPCS detector to direct illumination. The scattered signal travels through a 200 μm silicon filter, reducing the scattered signal by a factor of 14.5 [35] which allows simultaneous recording of XPCS data and collection of more photon-hungry diagnostics in chamber diagnostics such as x-ray Thomson scattering and x-ray diffraction. The scattered x-rays travel to

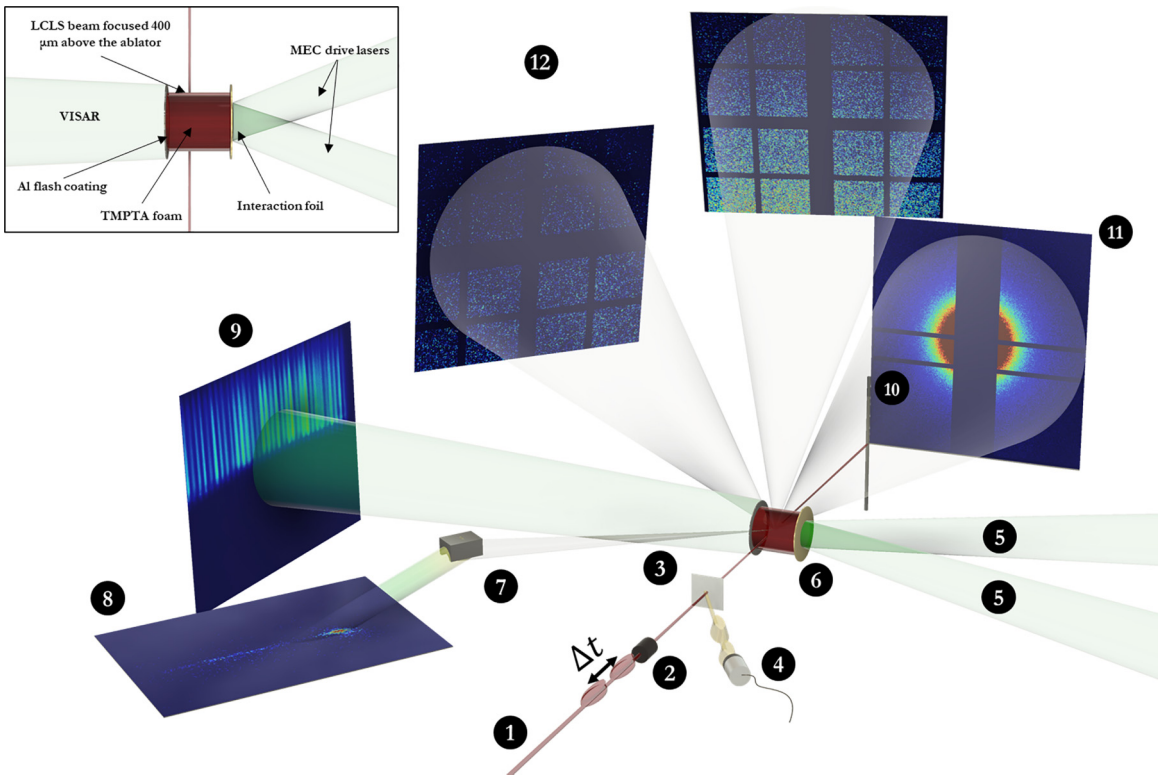

FIG. 1. Experimental layout. **1**: The LCLS beam, **2**: CRL focusing stack, **3**: Fe foil, **4**: Fast photodiode, **5**: MEC drive lasers, **6**: TMPTA foam target with the surrounding Kapton cylinder, **7**: HAPG dispersive crystal, **8**: ePix 100 detector capturing x-ray Thomson Scattering, **9**: VISAR, **10**: Beamblock, **11**: ePix 100 detector capturing x-ray speckle pattern, **12**: Pair of ePix10k quads capturing x-ray diffraction.

the XPCS detector, an ePix 100, placed $d = 4.6$ m away from the sample to record small angle x-ray scattering. The large sample to detector separation allows for the speckles to be large enough to be resolved on 50 μm pixels. The estimated speckle size is $S = \frac{\lambda d}{\sigma} \approx 70$ μm where $\lambda = 1.51$ Å for 8.2 keV photons.

III. RESULTS

A. Quantification of plasma properties

1. VISAR analysis

VISAR is fielded as both a pressure measurement and to time the XFEL beam to probe after the shock has passed the x-ray probe volume. Figure 3 shows the breakout time recorded from foams of differing heights. A linear fit is used to obtain a shock speed of $U_S = 10.9 \pm 0.4$ km s^{-1}.We calculate pressure following Paddock *et al.* (2023) [36], who showed that the principal Hugoniot for TMPTA foams can be adequately modeled by a homogeneous plastic equation of state. We therefore map the shock speed to a particle velocity of $U_P = 6.4 \pm 0.2$ km s^{-1} using Hyades generated QEOS tables for TMPTA [37]. Using the Rankine-Hugoniot equations, we infer a pressure of $P = P_0 + \rho_0 U_S U_P = 34 \pm 2$ GPa and a compression ratio of $\rho/\rho_0 = U_S/(U_S - U_P) = 2.4 \pm 0.2$, which implies a mass density of $\rho = 1.2 \pm 0.1$ g cm^{-3}. To ensure we probe the foam after the shock has passed, the first x-ray pulse is timed to arrive ∼40 ns after the laser ablation has started and is focused 400 μm above the interaction foil, see inset of Fig. 1.

2. X-ray Thomson scattering

X-ray Thomson scattering is capable of characterizing dense plasma states by measuring the dispersion of an x-ray probe after it travels through a plasma. Sheffield *et al.* (2010) [38] define the scattering cross section for photons with initial photon momentum $\hbar\mathbf{q}_0$ and scattered momentum $\hbar\mathbf{q}_1$ (with momentum transfer $\mathbf{q} = \mathbf{q}_1 - \mathbf{q}_0$) and scattered energy $\hbar\omega$ in solid angle Ω as

$$\frac{\mathrm{d}^2\sigma}{\mathrm{d}\Omega \mathrm{d}\omega} = \sigma_T \frac{|\mathbf{q}_1|}{|\mathbf{q}_0|} S(q, \omega), \tag{7}$$

where σ_T is the Thomson cross section, $q = |\mathbf{q}|$ and $S(q, \omega)$ is the dynamic structure factor, itself the time Fourier transform of the intermediate scattering function, defined in Eq. (3). The back-scattered spectrometer consists of a highly annealed pyrolytic graphite (HAPG) spherically bent crystal (51.7 mm radius of curvature) that spectrally disperses and focuses the scattered x-rays onto an ePix100 detector. Noncollective scattering is observed at 166° ($q = 8.2$ Å^{-1}), see Fig. 1. $S(q, \omega)$ can be written as a combination of elastic scattering due to electrons tightly bound to ions, $S_{ii}(q, \omega)$, and inelastic scattering due to free electrons, $S_{ee}(q, \omega)$. Paddock *et al.* (2023) [36] utilize streaked optical pyrometry to directly measure the temperature of laser shocked TMPTA foams and find that a foam shocked to 44.4 GPa is heated to 0.6 eV. The foams used in Paddock *et al.* have a lower initial density, 0.26 g cm^{-3}, than in our experiment so we expect that at 34 GPa foams we would reach a shocked temperature of $T \lesssim 0.6$ eV. This T precludes a temperature measurement from noncollective x-ray

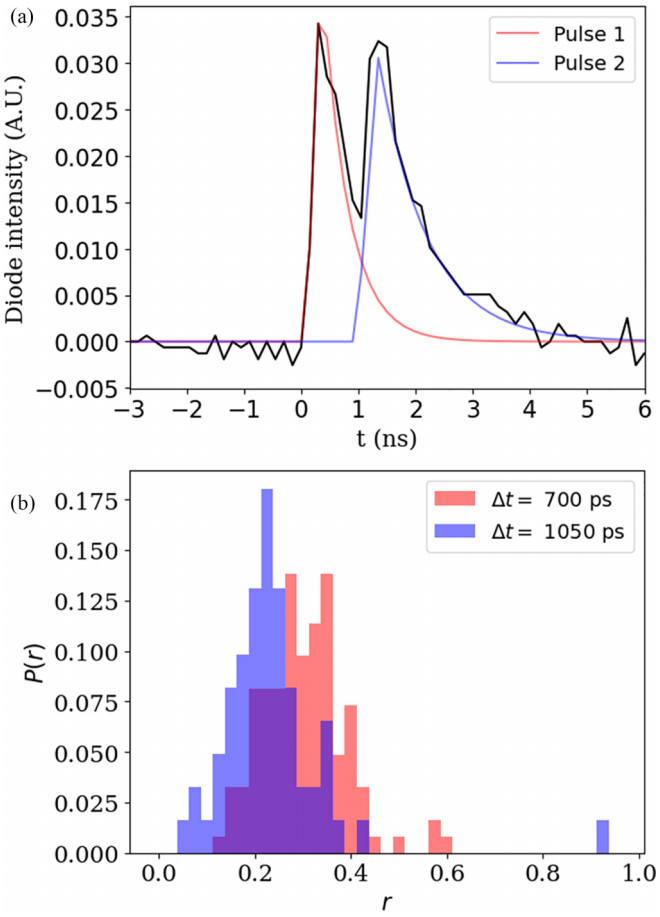

FIG. 2. Luminescence of an iron foil used as a transmissive pulse intensity diode. (a) Example of a two bunch mode separated by 1050 ps corresponding to $r = 0.24$. (b) Probability distribution of fitted r's for $\Delta t = 700$ ps and $\Delta t = 1050$ ps two bucket separations.

Thomson scattering, either from imaginary time correlation function thermometry [39] due to the broad source function or through fitting to a model for $S(q, \omega)$ [40] due to the plasma being Fermi degenerate, $\Theta = \frac{T_F}{T_e} > 5.2$. Ionization however can still be recovered by considering the ratio of inelastic, $I_i(q)$, to elastic scattering, $I_e(q)$:

$$\frac{I_i(q)}{I_e(q)} = \frac{Z_f \int_0^\infty S_{ee}(q,\omega)\mathrm{d}\omega}{|f_I(q) + Q(q)|^2 \int_0^\infty S_{ii}(q,\omega)\mathrm{d}\omega} = \frac{Z_f S_{ee}(q)}{|f_I(q) + Q(q)|^2 S_{ii}(q)}, \tag{8}$$

where Z_f is the number of free electrons (valence and ionized), $f_I(q)$ is the ionic form factor, and $Q(q)$ describes the screening cloud of electrons that surround the ions. In the non-collective regime, the approximation that $S_{ii}(q) = S_{ee}(q) \approx 1$ and $Q(q) \approx 0$ holds [40–42] and therefore

$$\frac{I_i(q)}{I_e(q)} \simeq \frac{Z_f}{|f_I(q)|^2}. \tag{9}$$

This applies to single species plasmas; for mixtures one finds that mean ionization is [43]

$$Z_f = \frac{I_i(q)}{I_e(q)} \sum_{a,b} \sqrt{w_a w_b} f_a(q) f_b(q), \tag{10}$$

where f_j and w_j are the ionic form factor and concentration of species j, respectively. Figure 4(a.1) shows x-ray Thomson scattering data 42 ns after the laser drive begins. The elastic and inelastic scattering contributions are separated allowing for a calculation of Z_f. Figure 4(a.2) indicates an increase in Z_f after the shock reaches the probe volume 37 ns after laser drive. While we note that Z_f increases after the shock, we do not expect that inelastic x-ray scattering significantly degrade contrast in the small angle x-ray scattering regime as $I_i(q) \to 0$ with small q.

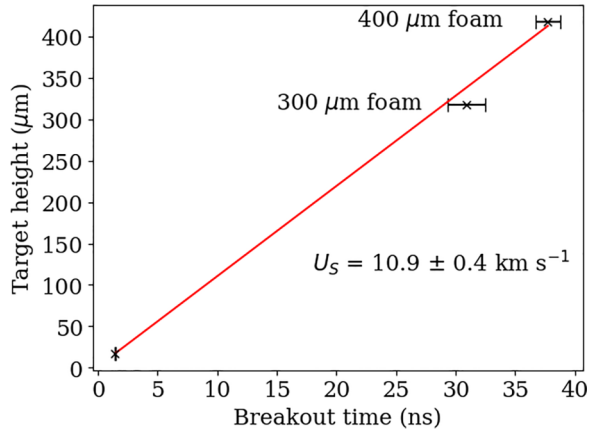

FIG. 3. Shock breakout time for foams manufactured to different heights. An aluminium flash coating is added to the end of the target such that the VISAR reflectivity drops when the shock breaks out.

3. *X-ray diffraction*

X-ray diffraction can be used qualitatively to show densification of the foam in the wake of the shock. The x-ray diffraction signal is corrected for the polarization of the XFEL, attenuation of the filters over the detector and for solid angle for each pixel before being azimuthally integrated. Figure 4(b.1) shows a comparison between the x-ray diffraction signal for ambient and shocked, probed 40 ns after the laser drive commences, samples. Under shock, a broad scattering peak emerges at $q = 2.11 \pm 0.18$ Å^{-1}, indicative of an amorphous/liquid structure at higher compression.

The ambient and shocked signals have significant contributions from the Kapton wall encapsulating the targets and so powder x-ray diffraction of a foam sample was carried out to reveal a single amorphous peak at $q = 1.27 \pm 0.31$ Å^{-1}; see the Supplemental Material for details [44]. Figure 4(b.2) shows a comparison between a powdered x-ray diffraction of an ambient sample and the change in signal under shock,

$$\Delta I(q) = I^{\text{Shocked}}(q)/I_0^{\text{Shocked}} - I^{\text{Ambient}}(q)/I_0^{\text{Ambient}}, \tag{11}$$

where I_0 is the probe intensity taken from the x-ray gas monitor. Despite the shift of the amorphous peak between the powdered TMPTA and the shocked foam, we cannot provide a measurement of mass density due to the low q coverage and the inability to rigorously subtract the ambient contribution. If one attributes the shift in peak from 1.27 Å^{-1} to 2.11 Å^{-1} to

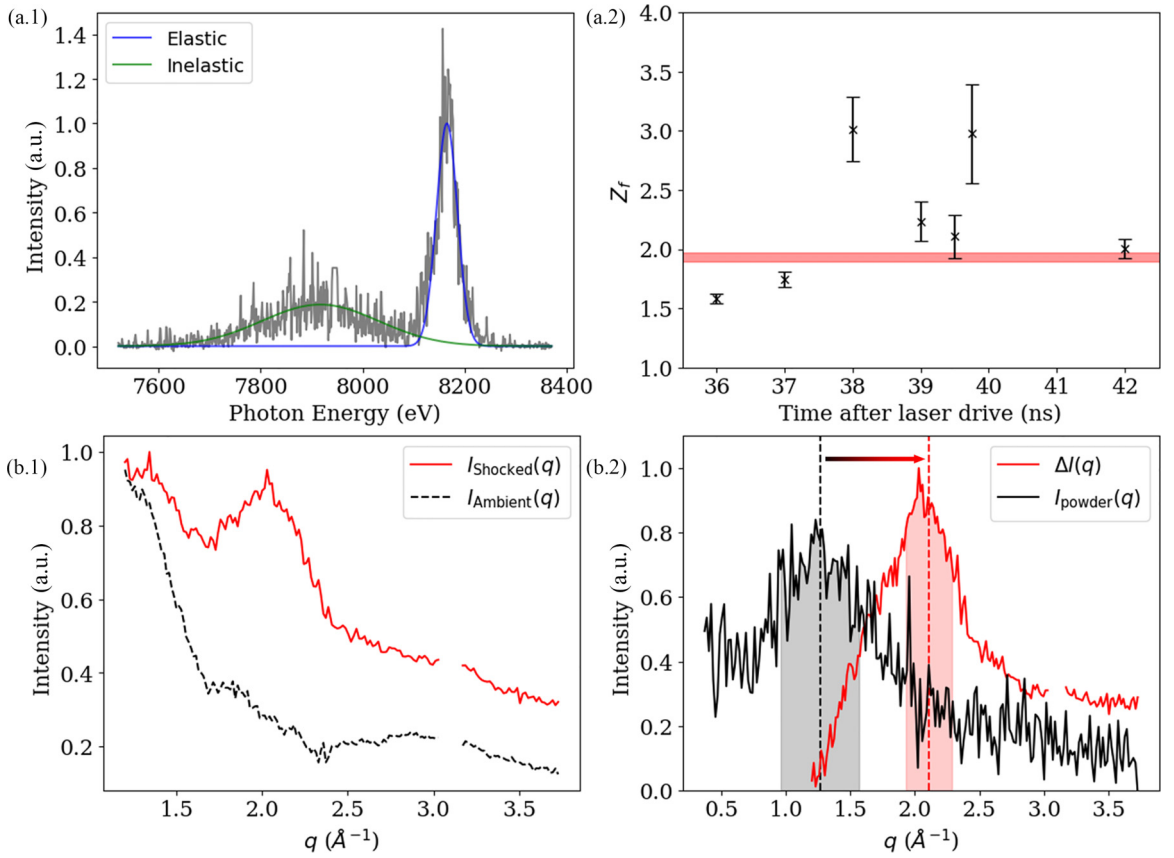

FIG. 4. X-ray diffraction and x-ray Thomson scattering are used to diagnose plasma conditions. (a.1) Noncollective x-ray Thomson Scattering separated by elastic and inelastic contributions. A Gaussian line shape is used to model both contributions. (a.2) Time series of Z_f. The shaded red region shows the derived Z_f for the ambient foam and its associated standard deviation across 7 x-ray only shots. (b.1) X-ray diffraction shows a clear indication of the shock compressing the foam with the appearance of an amorphous peak at $q = 2.11 \pm 0.18$ Å^{-1}. (b.2) Comparison between ambient powder x-ray diffraction and the change in signal under shock reveals a shift of an amorphous peak to higher q. The powder x-ray diffraction data is interpolated to match the spacing of the LCLS data. For the raw data, see the Supplemental Material [44].

uniform compression, mass density in the bulk TMPTA would increase by a factor of $(2.11$ Å$^{-1}/\ 1.27$ Å$^{-1})^3 = 4.48$. This is too high to be reasonable for a single shock at 34 GPa. We therefore can conclude that the shift in the peak is too great to be solely down to uniform compression of an ambient phase; the TMPTA must undergo a phase change. The x-ray diffraction analysis reveals compression predicted from VISAR does not arise from pore collapse alone but also through a change in the structure of the bulk TMPTA making up the foam.

B. Analysis of coherent x-ray speckle patterns

1. Determination of speckle contrast

To conduct XSVS, the contrast of the speckle pattern needs to be extracted. This is done by noting that in a speckle pattern the number of photons detected at a pixel position, is expected to follow a Γ distribution [45]

$$P(k|\bar{k},\beta) = \frac{\left(\frac{1}{\beta}\right)^{\frac{1}{\beta}}\left(\frac{k}{\bar{k}}\right)^{\frac{1}{\beta}-1}\exp\left(-\frac{k}{\bar{k}\beta}\right)}{\Gamma(\beta^{-1})}, \qquad (12)$$

where $\bar{k}$ is the mean photon count in a region of interest. This definition of β can be shown to be consistent with Eq. (4) by taking moments of Eq. (12); see the Supplemental Material [44]. In practice, $P(k|\bar{k},\beta)$ is a continuous distribution and does not fit the pixelated data well and so we employ a discrete Γ as defined in Chakraborty *et al.* (2012) [46]. Similarly, the Poisson-Γ distribution, commonly used in XSVS literature [47,48], is not suitable as we are not in the sparse photon limit.

Figure 5 demonstrates our approach to extracting contrast from the speckle patterns. Contrast at a scattering vector q is defined by taking eight radial regions and eight azimuthal regions for $0.006 < q < 0.013$ Å^{-1} and fitting photon statistics of those regions of interest to the discretized Γ distribution with $\beta(q)$ defined as the mean of the β's fitted in each region of interest for a $q \in [q - dq, q + dq]$ and errors defined by taken from the standard deviation across the azimuthal samples. Figure 5(c) plots the extracted contrast for an ambient TMPTA foam and after the passage of the shock for $\Delta t = 700$ ps. One observes that the contrast is high, especially for high q, and that there is a reduction for samples under motion (i.e. shocked). This is to be expected and forms the basis for our calculation of $|F(\mathbf{q},\tau)|^2$.

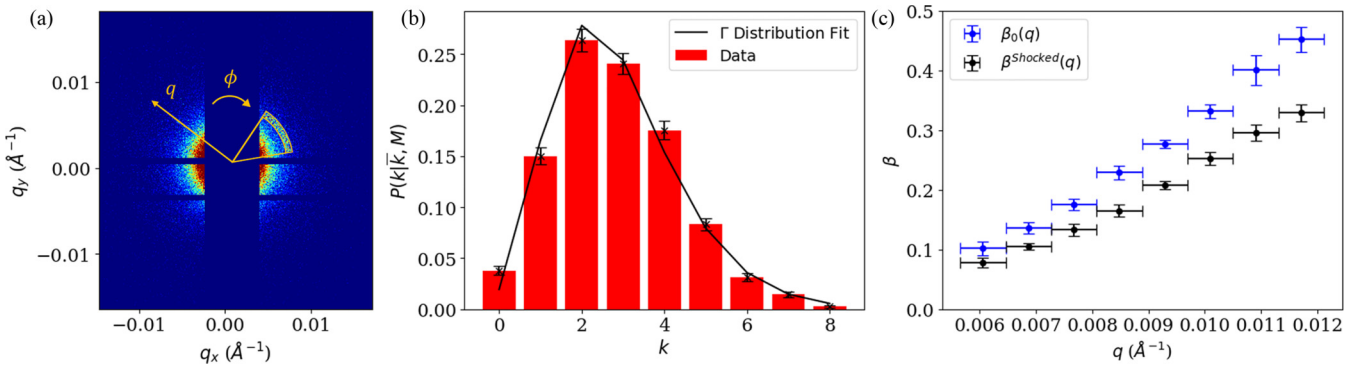

FIG. 5. Analysis of XPCS Data: (a) Partially annular region of interest highlighted. (b) Photon statistics in the highlighted region fitted to the discrete Γ distribution. (c) Comparison of $\beta(q)$ for an ambient and shocked foam for $\Delta t = 700$ ps.

2. *Model for* $|F(\mathbf{q}, \Delta t)|^2$

To extract transport properties from XSVS data, a model for $|F(\mathbf{q}, \tau)|^2$ is required. While low shear rates [25,49] have been studied, in the wake of a shock traversing a foam, one expects a turbulent flow [50,51]. We therefore employ the theory of Yin *et al.* [52] that describes XPCS in the case of a multi-scale turbulent flow. This assumes isotropic turbulence thus $F(\mathbf{q}, \tau)$ only depends on $q = |\mathbf{q}|$:

$$|F(q, \Delta t)|^2 = \exp\left[-\left(\frac{v_0 \Delta t}{\sigma}\right)^2\right] \exp[-(\delta v\, q\, \Delta t)^2] \times |F(q, \Delta t)_{\text{Plasma}}|^2, \tag{13}$$

where v_0 is the average particle velocity and δv is the turbulent velocity. $|F(q, \Delta t)_{\text{Plasma}}|^2$ describes the density fluctuations on a microscopic scale. Mithen *et al.* (2011) [53] argue that for length-scales that satisfy $\lambda_s q < 0.43$, where λ_s is the plasma screening length, a hydrodynamic description for density fluctuations can be used. For a degenerate system, $\lambda_s \approx \frac{1}{k_F} = 0.8$Å, where k_F is the Fermi wavevector, so $q_{\max}\lambda_s = 0.013\text{Å}^{-1} \times 0.8\text{Å} = 0.001$ and we are justified using this assumption. We further simply Mithen's model by assuming that time evolution of density perturbations is solely influenced from thermal diffusivity, see the Supplemental Material [44], giving

$$|F(q, \Delta t)_{\text{Plasma}}|^2 = \exp(-2D_T q^2 \Delta t), \tag{14}$$

where D_T is thermal diffusivity. To distinguish between turbulence and diffusivity, Eq. (13) requires that we have measurements of $|F(q, \Delta t)|^2$ over a range of scattering vectors and for more than one time separation.

3. *Calculation and interpretation of* $|F(q, \Delta t)|^2$

To extract $|F(q, \Delta t)|^2$ a comparison needs to be made between the contrast of a shocked sample and a stationary sample. For a stationary sample probed by two pulses, the only degradation in contrast from β_0 is due to spatial overlap and pulse intensity mismatch. It follows from Eq. (6) that

$$\beta_0(q) = \frac{\beta^{\text{Ambient}}(q)}{r^2 + (1-r)^2 + 2r(1-r)\mu}. \tag{15}$$

Substituting β_0 into Eq. (5) we get

$$|F(q, \Delta t)|^2 = \frac{1}{2r(1-r)\mu}[(r^2 + (1-r)^2 + 2r(1-r)\mu) \times \frac{\beta^{\text{Shocked}}(q, \Delta t)}{\beta^{\text{Ambient}}(q)} - r^2 - (1-r)^2]. \tag{16}$$

The spatial overlap, μ, is found to be the value that minimizes the parameter

$$\delta = \sqrt{\left[\frac{v_0^{(\text{fit})} - U_P}{\sigma_{U_P}}\right]^2 + \left[\frac{\sigma_{v_0}^{(\text{fit})}}{v_0^{(\text{fit})}}\right]^2}, \tag{17}$$

where v_0^{fit} is the fitted transit velocity from Eq. (13), U_P is the particle velocity inferred from VISAR and σ is the error associated with both velocities when $|F(q, \Delta t)|^2$ is fitted to Eq. (13). We find $\mu = 0.60$ for $\Delta t = 700$ ps separation and $\mu = 0.84$ for $\Delta t = 1050$ ps separation; see the Supplemental Material for details [44]. Now that intensity ratios and spatial overlap have been characterized, $F(q, \Delta t)$ can be recalculated using Eq. (16). Care is taken to ensure that conditions in the two shots are consistent. Drive energies and probe times were similar for both 700 ps and 1050 ps shots: 76.8 J and 40.25 ns and 77.6 J and 41 ns for 700 ps and 1050 ps shots,

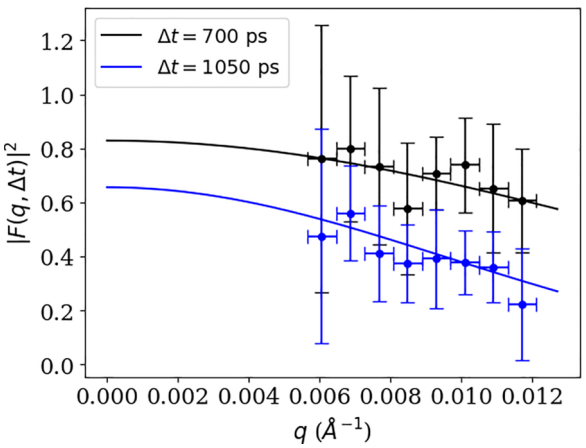

FIG. 6. $|F(q, \Delta t)|^2$ calculation at $\Delta t = 700$, 1050 ps. Best fits are found by modeling $|F(q, \Delta t)|^2$ to the isotropic turbulence model defined in Eq. (13).

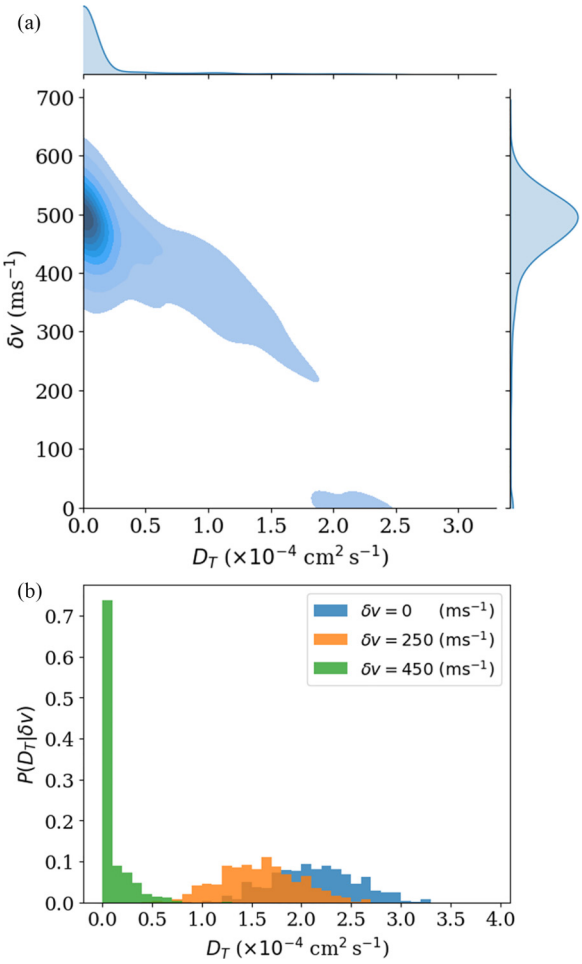

FIG. 7. Analysis of the fits of $|F(q,\tau)|^2$ to the isotropic turbulence model gives predictions for δv and bounds for D_T. (a) Mote Carlo sampling of fits of the isotropic turbulence model to the XSVS data. (b) Histogram of recovered thermal diffusivities having assumed different turbulent velocities.

respectively. A transmissive x-ray spectrometer [54], see the Supplemental Material [44], is used to ensure spectral quality which shows a narrow seeded spike for both shots. Figure 6 shows the intermediate scattering function at two times over a range of scattering vectors; a fit using the isotropic turbulence model is provided. To extract D_T and δv, the decay constant, $C = 2(D_T \Delta t + \delta v^2 \Delta t^2)$, is found for 700 ps and 1050 ps separation. Monte Carlo sampling of Fig. 6 reveals that the decay of $|F(q,\Delta t)|^2$ is dominated by the turbulent velocity term, as illustrated by Fig. 7. This allows us to only place upper bounds on the thermal diffusivity.

Figure 7 demonstrates that δv can be calculated to be 477 ± 112 m s^{-1}, whereas $D_T \leqslant 3 \times 10^{-4}$ cm^{-2} s^{-1}.

To compare this to literature, the Stanton Murillo transport model for electron thermal conductivity predicts that for a CH system at a density of 1 g cm^{-3}, $D_T < 3 \times 10^{-2}$ cm^2 s^{-1}. which is a significantly less restrictive bound than that found in our experiment. However, due to the $T^{5/2}$ scaling of thermal conductivity in a plasma, it is not expected that we have an exact match to a theory without a robust temperature measurement. To gain a better sensitivity for D_T, experiments at higher q could be performed [52]—however, this may suffer from poor signal to noise and so it would have to be a high repetition experiment. As for turbulent velocity, a parameter scan carried out by Davidovits *et al.* (2022) [51] on the turbulence left in the wake of shock traversing a porous medium predicts the empirical relation

$$\delta v \approx 0.52\ (R_{\mathrm{Pore}}/45\ \mu\mathrm{m})^{1/3} \overline{A} U_S, \tag{18}$$

where R_{Pore} is the pore radius and $\overline{A}$ is the average Atwood number in the preshocked region. This empirical formula predicts for our shocked foams, $R_{\mathrm{Pore}} \approx 1$ μm and $\overline{A} \approx 0.5$, $U_S = 10.9$ km s^{-1} will generate a turbulent wake with $\delta v \approx 800$ ms^{-1}. However, it is important to point out that [51] looked at pores of larger radius, $R > 23$ μm, at lower densities, $\rho = 0.05$ g cm^{-3} and at higher Mach numbers, $M > 12$ — for reference, we expect our laser drive to produce $M \approx 5.5$ shocks, assuming ambient $c_s \approx 2$ km s^{-1}. Despite these discrepancies, turbulent velocities found in this empirical model are of a similar order of magnitude to our experiment.

Our experimental platform thus offers a novel opportunity to leverage the MEC's high x-ray brightness, double bunch structure and drive lasers to diagnose transport and submicron scale flow characteristics of laser shock compressed materials.

ACKNOWLEDGMENTS

This work was performed at the Matter at Extreme Conditions (MEC) instrument of LCLS, supported by the DOE Office of Science, Fusion Energy Science under Contract No. SF00515. Use of the Linac Coherent Light Source (LCLS), SLAC National Accelerator Laboratory, is supported by the U.S. Department of Energy, Office of Science, Office of Basic Energy Sciences under Contract No. DE-AC02-76SF00515. This work was supported by Grant No. DE-NA0004134 under the DOE SC-NNSA Joint Program in HEDLP, and CMAP, an NSF Physics Frontiers Center, under Grant No. PHY-2020249. C.H. is grateful for funding and support from Trinity College Oxford's Whitehead scholarship and general academic grant and grants from the CLF's UK Hub for the Physical Sciences on XFELs. C.C. acknowledges support from the UK EPSRC under Grant No. EP/W010097/1. T.S. appreciates support from AWE via the Oxford Centre for High Energy Density Science (OxCHEDS). Partial support from Grants No. DE-NA0003914, No. PHY-2206380, No. CBET-2143702, No. DE-SC0019329, No. DE-SC0020229, and No. DE-NA0004144, and computing resources by the National Energy Research Scientific Computing Center (NERSC) under Contract No. DE-AC02-05CH11231 are also acknowledged. This material is based upon work supported by the Department of Energy [National Nuclear Security Administration] University of Rochester "National Inertial Confinement Fusion Program" under Award No. DE-NA0004144.

DATA AVAILABILITY

The data that support the findings of this article are openly available [55].

[1] C. R. Weber, D. S. Clark, A. W. Cook, L. E. Busby, and H. F. Robey, Inhibition of turbulence in inertial-confinement-fusion hot spots by viscous dissipation, Phys. Rev. E **89**, 053106 (2014).

[2] T. Guillot, Interiors of giant planets inside and outside the solar system, Science **286**, 72 (1999).

[3] T. Guillot, Y. Miguel, B. Militzer, W. Hubbard, Y. Kaspi, E. Galanti, H. Cao, R. Helled, S. Wahl, L. Iess *et al.*, A suppression of differential rotation in Jupiter's deep interior, Nature (London) **555**, 227 (2018).

[4] P. E. Grabowski, S. B. Hansen, M. S. Murillo, L. G. Stanton, F. R. Graziani, A. B. Zylstra, S. D. Baalrud, P. Arnault, A. D. Baczewski, L. X. Benedict, C. Blancard, O. Čertík, J. Clérouin, L. A. Collins, S. Copeland, A. A. Correa, J. Dai, J. Daligault, M. P. Desjarlais, M. W. Dharma-wardana *et al.*, Review of the first charged-particle transport coefficient comparison workshop, in *High Energy Density Physics* (Elsevier B.V., Amsterdam, 2020), Vol. 37.

[5] L. J. Stanek, A. Kononov, S. B. Hansen, B. M. Haines, S. X. Hu, P. F. Knapp, M. S. Murillo, L. G. Stanton, H. D. Whitley, S. D. Baalrud, L. J. Babati, A. D. Baczewski, M. Bethkenhagen, A. Blanchet, R. C. Clay, K. R. Cochrane, L. A. Collins, A. Dumi, G. Faussurier, M. French *et al.*, Review of the second charged-particle transport coefficient code comparison workshop, Phys. Plasmas **31**, 052104 (2024).

[6] E. Abramson, J. Brown, L. Slutsky, and S. Wiryana, Measuring speed of sound and thermal diffusivity in the diamond-Anvil cell, Int. J. Thermophys. **22**, 405 (2001).

[7] A. F. Goncharov, P. Beck, V. V. Struzhkin, B. D. Haugen, and S. D. Jacobsen, Thermal conductivity of lower-mantle minerals, Phys. Earth Planet. Inter. **174**, 24 (2009).

[8] Y. Zhou, Z. Y. Dong, W. P. Hsieh, A. F. Goncharov, and X. J. Chen, Thermal conductivity of materials under pressure, Nature Rev. Phys. **4**, 319 (2022).

[9] C. H. Allen, M. Oliver, D. O. Gericke, N. Brouwer, L. Divol, G. E. Kemp, O. L. Landen, L. Morrison, Y. Ping, M. O. Schölmerich *et al.*, Measurement of interfacial thermal resistance in high-energy-density matter, Nat. Commun. **16**, 1983 (2025).

[10] S. Jiang, O. L. Landen, H. D. Whitley, S. Hamel, R. London, D. S. Clark, P. Sterne, S. B. Hansen, S. X. Hu, G. W. Collins, and Y. Ping, Thermal transport in warm dense matter revealed by refraction-enhanced x-ray radiography with a deep-neural-network analysis, Commun. Phys. **6**, 98 (2023).

[11] V. Favre-Nicolin, Y. Chushkin, P. Cloetens, J. da Silva, S. Leake, B. Ruta, and F. Zontone, Dynamics and imaging using coherent x-rays at the european synchrotron, Synchrotron Radiat. News **30**, 13 (2017).

[12] O. G. Shpyrko, X-ray photon correlation spectroscopy, J. Synchrotron Radiat. **21**, 1057 (2014).

[13] A. R. Sandy, Q. Zhang, and L. B. Lurio, Hard x-ray photon correlation spectroscopy methods for materials studies, Annu. Rev. Mater. Res. **48**, 167 (2018).

[14] G. Grübel, G. B. Stephenson, C. Gutt, H. Sinn, and T. Tschentscher, Xpcs at the european x-ray free electron laser facility, Nucl. Instrum. Methods Phys. Res., Sect. B **262**, 357 (2007).

[15] F. Lehmkühler, P. Kwasniewski, W. Roseker, B. Fischer, M. A. Schroer, K. Tono, T. Katayama, M. Sprung, M. Sikorski, S. Song, J. Glownia, M. Chollet, S. Nelson, A. Robert, C. Gutt, M. Yabashi, T. Ishikawa, and G. Grübel, Sequential single shot x-ray photon correlation spectroscopy at the sacla free electron laser, Sci. Rep. **5**, 17193 (2015).

[16] W. Roseker, S. O. Hruszkewycz, F. Lehmkühler, M. Walther, H. Schulte-Schrepping, S. Lee, T. Osaka, L. Strüder, R. Hartmann, M. Sikorski, S. Song, A. Robert, P. H. Fuoss, M. Sutton, G. B. Stephenson, and G. Grübel, Towards ultrafast dynamics with split-pulse x-ray photon correlation spectroscopy at free electron laser sources, Nat. Commun. **9**, 1704 (2018).

[17] B. J. Berne and R. Pecora, *Dynamic Light Scattering: With Applications to Chemistry, Biology, and Physics* (Courier Corporation, North Chelmsford, MA, 2000).

[18] A. Cornet, A. Ronca, J. Shen, F. Zontone, Y. Chushkin, M. Cammarata, G. Garbarino, M. Sprung, F. Westermeier, T. Deschamps *et al.*, High-pressure x-ray photon correlation spectroscopy at fourth-generation synchrotron sources, J. Synchrotron Radiat. **31**, 527 (2024).

[19] P. Muhunthan, H. Li, G. Vignat, E. R. Toro, K. Younes, Y. Sun, D. Sokaras, T. Weiss, I. Rajkovic, T. Osaka *et al.*, A versatile pressure-cell design for studying ultrafast molecular-dynamics in supercritical fluids using coherent multi-pulse x-ray scattering, Rev. Sci. Instrum. **95**, 013901 (2024).

[20] A. Karina, H. Li, T. Eklund, M. Ladd-Parada, B. Massani, M. Filianina, N. Kondedan, A. Rydh, K. Holl, R. Trevorah *et al.*, Multicomponent dynamics in amorphous ice studied using x-ray photon correlation spectroscopy at elevated pressure and cryogenic temperatures, Commun. Chem. **8**, 82 (2025).

[21] D. Ferreira, R. Bachelard, W. Guerin, R. Kaiser, and M. Fouché, Connecting field and intensity correlations: The siegert relation and how to test it, Am. J. Phys. **88**, 831 (2020).

[22] J.-P. Hansen and I. R. McDonald, *Theory of Simple Liquids: With Applications to Soft Matter* (Academic Press, San Diego, CA, 2013).

[23] M. H. Seaberg, B. Holladay, J. C. T. Lee, M. Sikorski, A. H. Reid, S. A. Montoya, G. L. Dakovski, J. D. Koralek, G. Coslovich, S. Moeller, W.F. Schlotter, R. Streubel, S.D. Kevan, P. Fischer, E. E. Fullerton, J. L. Turner, F. J. Decker, S. K. Sinha, S. Roy, and J. J. Turner, Nanosecond x-ray photon correlation spectroscopy on magnetic skyrmions, Phys. Rev. Lett. **119**, 067403 (2017).

[24] A. Majumdar, H. Li, P. Muhunthan, A. Späh, S. Song, Y. Sun, M. Chollet, D. Sokaras, D. Zhu, and M. Ihme, Direct observation of ultrafast cluster dynamics in supercritical carbon dioxide using x-ray photon correlation spectroscopy, Nat. Commun. **15**, 10540 (2024).

[25] Y. Sun, G. Carini, M. Chollet, F.-J. Decker, M. Dunne, P. Fuoss, S. O. Hruszkewycz, T. J. Lane, K. Nakahara, S. Nelson, A. Robert, T. Sato, S. Song, G. B. Stephenson, M. Sutton, T. B. Van Driel, C. Weninger, and D. Zhu, Nonuniform flow dynamics probed by nanosecond x-ray speckle visibility spectroscopy, Phys. Rev. Lett. **127**, 058001 (2021).

[26] C. Gutt, L.-M. Stadler, A. Duri, T. Autenrieth, O. Leupold, Y. Chushkin, and G. Grübel, Measuring temporal speckle correlations at ultrafast x-ray sources, Opt. Express **17**, 55 (2009).

[27] B. Nagler, B. Arnold, G. Bouchard, R. F. Boyce, R. M. Boyce, A. Callen, M. Campell, R. Curiel, E. Galtier, J. Garofoli *et al.*, The matter in extreme conditions instrument at the linac coherent light source, J. Synchrotron Radiat. **22**, 520 (2015).

[28] Y. Sun, F.-J. Decker, J. Turner, S. Song, A. Robert, and D. Zhu, Pulse intensity characterization of the LCLS nanosecond

double-bunch mode of operation, J. Synchrotron Radiat. **25**, 642 (2018).

[29] J. Amann, W. Berg, V. Blank, F.-J. Decker, Y. Ding, P. Emma, Y. Feng, J. Frisch, D. Fritz, J. Hastings *et al.*, Demonstration of self-seeding in a hard-x-ray free-electron laser, Nat. Photon. **6**, 693 (2012).

[30] A. S. Moore, N. B. Meezan, J. Milovich, S. Johnson, R. Heredia, T. F. Baumann, M. Biener, S. D. Bhandarkar, H. Chen, L. Divol, N. Izumi, A. Nikroo, K. Baker, O. Jones, O. L. Landen, W. W. Hsing, J. D. Moody, C. A. Thomas, B. Lahmann, J. Williams *et al.*, Foam-lined Hohlraum, inertial confinement fusion experiments on the national ignition facility, Phys. Rev. E **102**, 051201(R) (2020).

[31] P. M. Celliers and M. Millot, Imaging velocity interferometer system for any reflector (visar) diagnostics for high energy density sciences, Rev. Sci. Instrum. **94**, 011101 (2023).

[32] H. Radousky, M. Armstrong, and N. Goldman, Time resolved x-ray diffraction in shock compressed systems, J. Appl. Phys. **129**, 040901 (2021).

[33] S. H. Glenzer and R. Redmer, X-ray thomson scattering in high energy density plasmas, Rev. Mod. Phys. **81**, 1625 (2009).

[34] F.-J. Decker, K. L. Bane, W. Colocho, S. Gilevich, A. Marinelli, J. C. Sheppard, J. L. Turner, J. J. Turner, S. L. Vetter, A. Halavanau *et al.*, Tunable x-ray free electron laser multi-pulses with nanosecond separation, Sci. Rep. **12**, 3253 (2022).

[35] B. L. Henke, E. M. Gullikson, and J. C. Davis, X-ray interactions: Photoabsorption, scattering, transmission, and reflection at E = 50-30,000 ev, Z = 1-92, At. Data Nucl. Data Tables **54**, 181 (1993).

[36] R. W. Paddock, M. W. von der Leyen, R. Aboushelbaya, P. A. Norreys, D. J. Chapman, D. E. Eakins, M. Oliver, R. J. Clarke, M. Notley, C. D. Baird, N. Booth, C. Spindloe, D. Haddock, S. Irving, R. H. H. Scott, J. Pasley, M. Cipriani, F. Consoli, B. Albertazzi, M. Koenig, A. S. Martynenko, L. Wegert, P. Neumayer, P. Tchorz, P. Raczka, P. Mabey, W. Garbett, R. M. N. Goshadze, V. V. Karasiev, and S. X. Hu, Measuring the principal hugoniot of inertial-confinement-fusion-relevant TMPTA plastic foams, Phys. Rev. E **107**, 025206 (2023).

[37] J. T. Larsen and S. M. Lane, Hyades—A plasma hydrodynamics code for dense plasma studies, J. Quant. Spectrosc. Radiat. Transfer **51**, 179 (1994), special issue radiative properties of hot dense matter.

[38] J. Sheffield, D. Froula, S. H. Glenzer, and N. C. Luhmann, Jr., *Plasma Scattering of Electromagnetic Radiation: Theory and Measurement Techniques* (Academic Press, San Diego, CA, 2010).

[39] T. Dornheim, M. P. Böhme, D. A. Chapman, D. Kraus, T. R. Preston, Z. A. Moldabekov, N. Schlünzen, A. Cangi, T. Döppner, and J. Vorberger, Imaginary-time correlation function thermometry: A new, high-accuracy and model-free temperature analysis technique for x-ray thomson scattering data, Phys. Plasmas **30**, 042707 (2023).

[40] G. Gregori, S. H. Glenzer, W. Rozmus, R. W. Lee, and O. L. Landen, Theoretical model of x-ray scattering as a dense matter probe, Phys. Rev. E **67**, 026412 (2003).

[41] A. Pelka, G. Gregori, D. O. Gericke, J. Vorberger, S. H. Glenzer, M. M. Günther, K. Harres, R. Heathcote, A. L. Kritcher, N. L. Kugland, B. Li, M. Makita, J. Mithen, D. Neely, C. Niemann, A. Otten, D. Riley, G. Schaumann, M. Schollmeier, A. Tauschwitz, and M. Roth, Ultrafast melting of carbon induced by intense proton beams, Phys. Rev. Lett. **105**, 265701 (2010).

[42] J. Lütgert, P. Hesselbach, M. Schörner, V. Bagnoud, R. Belikov, P. Drechsel, B. Heuser, O. Humphries, P. Katrik, B. Lindqvist *et al.*, Temperature and structure measurements of heavy-ion-heated diamond using in situ x-ray diagnostics, Matter Radiat. Extremes **9**, 047802 (2024).

[43] K. Wünsch, J. Vorberger, G. Gregori, and D. O. Gericke, X-ray scattering as a probe for warm dense mixtures and high-pressure miscibility, Europhys. Lett. **94**, 25001 (2011).

[44] See Supplemental Material at http://link.aps.org/supplemental/10.1103/lff9-f3c1 for information on the source monitor to verify self-seeding spectrum, derivation of the model for $F_{\text{plasma}}(q,\tau)$, fitting for the spatial overlap, derivation of the speckle intensity distribution, moments of the speckle intensity distribution function and powder x-ray diffraction of ambient TMTPA.

[45] J. W. Goodman, Statistical properties of laser speckle patterns, in *Laser Speckle and Related Phenomena* (Springer, Berlin, 1975), pp. 9–75.

[46] S. Chakraborty and D. Chakravarty, Discrete gamma distributions: Properties and parameter estimations, Commun. Stat. Theory Methods **41**, 3301 (2012).

[47] Y. Sun, J. Montana-Lopez, P. Fuoss, M. Sutton, and D. Zhu, Accurate contrast determination for x-ray speckle visibility spectroscopy, J. Synchrotron Radiat. **27**, 999 (2020).

[48] S. O. Hruszkewycz, M. Sutton, P. H. Fuoss, B. Adams, S. Rosenkranz, K. F. Ludwig Jr, W. Roseker, D. Fritz, M. Cammarata, D. Zhu, S. Lee, H. Lemke, C. Gutt, A. Robert, G. Grubel, and G. B. Stephenson, High contrast x-ray speckle from atomic-scale order in liquids and glasses, Phys. Rev. Lett. **109**, 185502 (2012).

[49] S. Busch, T. H. Jensen, Y. Chushkin, and A. Fluerasu, Dynamics in shear flow studied by x-ray photon correlation spectroscopy, Eur. Phys. J. E **26**, 55 (2008).

[50] H.-C. Li and R. W. Houim, Pore-scale resolved simulation of quenching, acceleration, and transition to detonation of hydrogen explosions by metal foams, Combust. Flame **259**, 113118 (2024).

[51] S. Davidovits, C. Federrath, R. Teyssier, K. S. Raman, D. C. Collins, and S. R. Nagel, Turbulence generation by shock interaction with a highly nonuniform medium, Phys. Rev. E **105**, 065206 (2022).

[52] H. Yin, C. Heaton, E. G. Blackman, A. E. Gleason, J. J. Turner, G. W. Collins, G. Gregori, J. K. Shang, and H. Aluie, Theory of x-ray photon correlation spectroscopy for multiscale flows, Phys. Rev. Res. **7**, 023202 (2025).

[53] J. P. Mithen, J. Daligault, and G. Gregori, Extent of validity of the hydrodynamic description of ions in dense plasmas, Phys. Rev. E **83**, 015401(R) (2011).

[54] D. Zhu, M. Cammarata, J. M. Feldkamp, D. M. Fritz, J. B. Hastings, S. Lee, H. T. Lemke, A. Robert, J. L. Turner, and Y. Feng, A single-shot transmissive spectrometer for hard x-ray free electron lasers, Appl. Phys. Lett. **101**, 034103 (2012).

[55] C. Heaton and G. Gregori, Dataset for Measurement of turbulent velocity and bounds for thermal diffusivity in laser shock compressed foams by X-ray photon correlation spectroscopy (University of Oxford, 2025), https://dx.doi.org/10.5287/ora-brnr9da2n.